



HAL
open science

Clay Minerals in the Deep Reservoir of the Cerro Pabellón Geothermal System (Northern Chile)

Jeanne Vidal, Patricia Patrier, Daniel Beaufort, Santiago Maza, Germain Rivera, Gianni Volpi, Diego Morata

► **To cite this version:**

Jeanne Vidal, Patricia Patrier, Daniel Beaufort, Santiago Maza, Germain Rivera, et al.. Clay Minerals in the Deep Reservoir of the Cerro Pabellón Geothermal System (Northern Chile). *Minerals*, 2022, 12 (10), pp.1244. 10.3390/min12101244 . hal-04157684

HAL Id: hal-04157684

<https://hal.science/hal-04157684>

Submitted on 12 Jul 2023

HAL is a multi-disciplinary open access archive for the deposit and dissemination of scientific research documents, whether they are published or not. The documents may come from teaching and research institutions in France or abroad, or from public or private research centers.



L'archive ouverte pluridisciplinaire **HAL**, est destinée au dépôt et à la diffusion de documents scientifiques de niveau recherche, publiés ou non, émanant des établissements d'enseignement et de recherche français ou étrangers, des laboratoires publics ou privés.



Distributed under a Creative Commons Attribution 4.0 International License

Article

Clay Minerals in the Deep Reservoir of the Cerro Pabellón Geothermal System (Northern Chile)

Jeanne Vidal ^{1,*}, Patricia Patrier ², Daniel Beaufort ², Santiago Maza ¹, Germain Rivera ³, Gianni Volpi ³ and Diego Morata ¹

¹ Department of Geology, Andean Geothermal Center of Excellence (CEGA), Facultad de Ciencias Físicas y Matemáticas, University of Chile, Santiago 8370450, Chile

² Department IC2MP, UMR 7285, University of Poitiers, 86073 Poitiers, France

³ ENEL Green Power Chile and Andean Countries, Santiago 8330099, Chile

* Correspondence: jeannevidal@ing.uchile.cl

Abstract: This study focuses on hydrothermal alteration, and more specifically clays, in the geothermal reservoir of Cerro Pabellón in Andean Cordillera, Northern Chile. Although it is the first commercial geothermal power plant in South America with 48 MWe installed and an additional 33 MWe during 2022, the alteration mineralogy of the deep reservoir remains poorly investigated. Cuttings from two deep wells drilled between 500 and 3000 m depth were sampled. The fine-grained clay fraction was analyzed using X-ray diffraction to observe the mineral distribution and variations of crystal structure of the clays. Scanning electron microscopy coupled with energy dispersive spectroscopy allowed us to perform microanalysis of the clays. The results suggest a high heterogeneity of the reservoir in term of alteration: a pervasive alteration dominated by trioctahedral clays was observed in all the samples, whereas a fracture-controlled alteration was only observed locally, dominated by dioctahedral clays. Illite-smectite mixed layers with more than 90% illite typically occur in permeable fracture and fault as a typical clay signature. This study completed an integrated conceptual model of the high enthalpy reservoir (>250 °C). Circulations of a neutral pH Na-K-Cl fluid occur in a wide fracture system connected to highly dipping and NW-striking faults and could extend beyond the Pabelloncito graben.

Keywords: high-enthalpy system; deep fluids; permeable fracture; clay minerals; hydrothermal alteration; Cerro Pabellón; Chile; Andean Cordillera



Citation: Vidal, J.; Patrier, P.; Beaufort, D.; Maza, S.; Rivera, G.; Volpi, G.; Morata, D. Clay Minerals in the Deep Reservoir of the Cerro Pabellón Geothermal System (Northern Chile). *Minerals* **2022**, *12*, 1244. <https://doi.org/10.3390/min12101244>

Academic Editors: Daniele Tardani, Marco Taussi and Jacopo Cabassi

Received: 29 August 2022

Accepted: 23 September 2022

Published: 29 September 2022

Publisher's Note: MDPI stays neutral with regard to jurisdictional claims in published maps and institutional affiliations.



Copyright: © 2022 by the authors. Licensee MDPI, Basel, Switzerland. This article is an open access article distributed under the terms and conditions of the Creative Commons Attribution (CC BY) license (<https://creativecommons.org/licenses/by/4.0/>).

1. Introduction

The Central Andean Volcanic Zone (CAVZ) represents one of the most important and mostly undeveloped geothermal areas, with no less than 300 geothermal systems associated with quaternary volcanism resulting from the subduction of the Nazca and Antarctic oceanic plates below South America [1,2]. Several active geothermal systems were identified such as El Tatio, La Torta, and Cerro Pabellón (CP) [1,3]. Discovered in 1999 (previously referred as the 'Apacheta geothermal project' by [4]), the CP geothermal system is located ~100 km northeast of Calama city (Antofagasta region, Northern Chile), near the border between Chile and Bolivia. Since 2017, Geotérmica del Norte, a joint venture between Enel Green Power Chile and ENAP (Chilean National Oil Company), has exploited this system with 13 wells at 4500 m a.s.l, a 48 MWe installed capacity power plant (two binary 24 MWe each one units), and an additional 33 MWe for 2022 [5]. The deep reservoir of ~5 × 5 km² between 500 and 2000 m depth is defined as a high-enthalpy (>250 °C) two-phase reservoir [1]. Previous geological studies were mainly conducted on surficial alteration and the 300 m thick clay cap, whereas the deep reservoir (>500 m depth) remains poorly investigated [6,7]. Although the Andean geothermal potential remains one of the highest in the world, the CP power plant is the only one in exploitation in South

America. Further exploration and investigation on deep hydrothermal circulations will help the development of geothermal projects in the Andean Cordillera.

This study identified hydrothermal alteration in cuttings from two deep wells in the reservoir part between 500 and 3000 m MD (measured depth). During the life of geothermal systems, the fluid circulations into the reservoir lead to dissolutions of primary minerals and glassy or fine-grained groundmass of volcanogenic host rocks and subsequent deposition of secondary minerals. The nature and amount of mineralogical parageneses associated with alteration of the deep rock samples could help to understand paleo and present-day circulations of the geothermal system [8–16]. As clay minerals are very sensitive to physico-chemical changes (temperature, F/R ratio, time, nature of hydrothermal fluids, fluid state), special attention was paid to the clay minerals [17–21].

The goal of the proposed study was to characterize the hydrothermal alteration in the active part of the CP geothermal system and to determine the clay signature of the fluid circulations which control the present-day productivity of the geothermal reservoir. Such a contribution may be of interest for other Andean geothermal systems with more limited geological information and may help in the further development of geothermal projects in the Chilean Andes and neighboring countries.

2. Geological Settings

Within the CAVZ, the CP geothermal system belongs to the graben structure called the Pabelloncito graben (Figure 1a). The geology of the area has been widely described by [7,22–25]. This depression of 20 km long and 3 km wide is framed between two main faults, N 53° W to N 60° W direction, and a secondary fault system in between with the same orientation affects the geological units (Figure 1b). It was initiated by a local Pliocene extensional phase that continued until the Holocene, with normal faults acting as structural weakness for extrusion of the dacitic lava domes [24,26–28]. This NW tectonic trend is commonly observed in the CAVZ for faults and lineaments and represents the main pathways for fluid migration towards shallower crustal levels [26,28–30]. In the Pabelloncito graben, the hydrothermal circulations are sealed upwards by a thick clay cap [4,6,24,31].

The 300 m-thick clay cap studied in the core samples of the exploration well PExAp-1 reveals an intensive, pervasive alteration dominated by smectite (montmorillonite-beidellite) associated to hematite, zeolites, calcite, and quartz [6]. A transition zone is identified below and corresponds to the transition from R0 to R3 illite-smectite mixed layers (I-S). The dioctahedral sequence is associated to chlorite-smectite mixed layers, corrensite, chlorite-corrensite mixed layers (C-Crr), and chlorite, Na-plagioclase, quartz, calcite, hematite, stilbite, and laumontite. Finally, the top of the reservoir (below 500 m depth) is dominated by illite and chlorite and associated with chlorite-corrensite mixed layers, epidote, Na-plagioclase, adularia, quartz, calcite, pyrite, chalcopyrite, and titanite.

An integrated conceptual model, including a diffuse CO₂ survey, was proposed by [7], confirming the strong control of the thick clay cap in the absence of surficial hydrothermal manifestations in the center of the graben. A few superheated fumaroles displaying high temperatures in the range of 108–119 °C, and a fossil alteration zone with pervasive hydrothermal alteration, were observed at ~5000–5200 m a.s.l. on the top of the Apacheta-Aguilucho Volcanic Complex at the NW of the graben [4,22,31,32] (Figure 1b). Poorly crystallized kaolinite and cristobalite (opal-C), alunite, alunogen, and Mg-Zn-Cu-rich smectite are associated in rocks of the active “fumaroles” zone, and the association of well-crystallized kaolinite, alunite-natroalunite, pyrophyllite, mixed opal-A-opal C/T-quartz and Mg-Zn-Cu-rich illite-smectite was identified in the fossil zone.

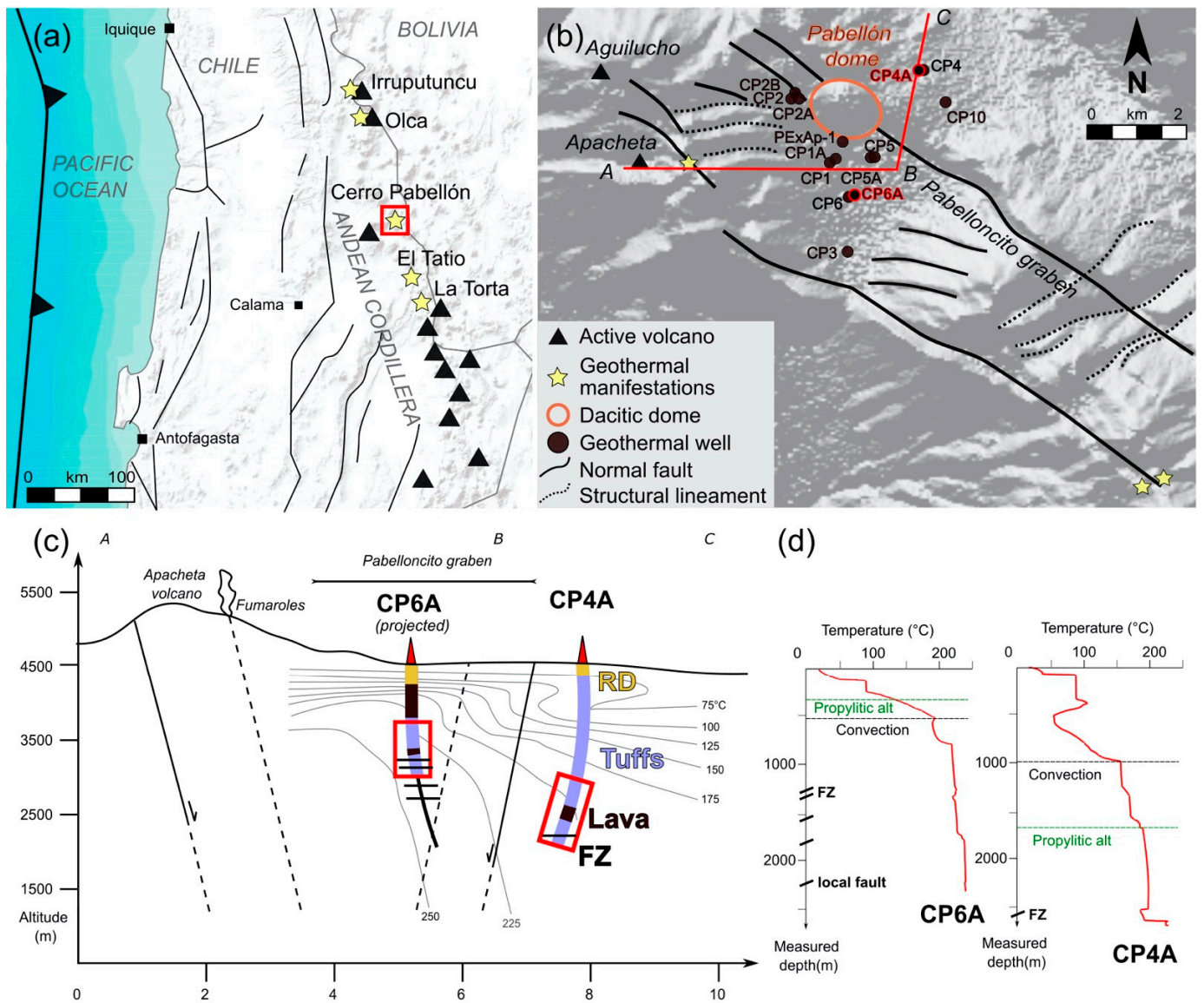


Figure 1. (a) Map of the Central Andean Volcanic Zone (CAVZ), regional scale faults, active volcanoes and main geothermal manifestations (geysers, fumaroles, steam grounds, hot springs, etc.) in the Chilean side after [1]. The image used in the background is from ESRI. The red square is the studied area, also detailed in (b): map of the Pabelloncito graben with geothermal wells, main faults and lineaments. The trace ABC in red is presented in (c): schematic profile with measured isotherms after [33]. The simplified geology and traces of the intersected fracture zones (FZ) and local faults are from [24,34]. The red rectangle is the studied zone in the paper. RD: recent deposits (unconsolidated deposits and ignimbrites); tuffs: lithic and dacitic tuffs; lava: andesitic lavas; red rectangles are the studied zone in this paper; the deep part of CP6A was not sampled because of circulation losses. (d) T profiles in CP4A and CP6A wells measured several months after drilling operations. FZ intersected and tops of convection and propylitic alteration are from [34].

Others warm springs with temperature around 23 °C were observed around 17 km SW of the power plant location [4] (Figure 1b). At the SE of the graben, the Cordón de Inacaliri area is characterized by steaming grounds and a scarce fumarolic activity associated with an extensive acid–sulphate (alunite + kaolinite + opal CT + anatase) to argillic alteration (kaolinite + hematite + halloysite + smectite + illite-smectite + illite) and CO₂ flux that allowed estimation of an electrical capacity potential of 1.08 MWe km⁻² [23,25].

The fluid circulating in the CP reservoir is a typical Na-K-Cl geothermal fluid with high solutes content and low gas content [33]. The recalculated pH at reservoir conditions is between 5 and 6.2. The Na-K geothermometer indicates apparent equilibrium temperatures in the range of 280–290 °C, higher than the 255 °C measured in the hotter wells, suggesting that the system could be even hotter at depth. As the downhole temperature was measured only several months after drilling, it could be that it was not at thermal equilibrium. The δD - $\delta^{18}O$ values suggest several millions of years of the fluid's mean residence time within the CP geothermal reservoir and strong interaction with the volcanogenic host rocks. In addition, the apparent ages of the geothermal fluid samples constrained using ^{14}C ages and 3H values also point to very long residence times for waters and a possible magmatic component [35]. The geochemical conceptual model suggests infiltration of meteoric waters that migrated from the recharge zone to the geothermal reservoir, interacting with volcanogenic host rocks at high temperatures (>250 °C) and mixed with a possible magmatic water [33].

The 3D thermal model of the CP reservoir shows a dome shape of the isotherms (Figure 1c) [34]. The apex of the thermal dome marks the center of the upflow zone of the geothermal fluid in the NW edge of the Pabelloncito graben. Wells from platforms CP-1, CP-5, and CP-6, drilled in this hot core of the system, present the greater production potential. On the margins of the upflow zone, temperature gradients decrease gradually towards the north (CP-2 platform) and the south (CP-3 platform), and more abruptly outside the graben towards the CP-4 and CP-10 platforms. The model proposed by [34] points out a good relationship of the thermal data, the propylitic facies, and the permeability distribution. The reservoir is associated with the propylitic facies described by [6] and a nearly vertical temperature (T) profile traducing a convective circulation of the fluid (Figure 1d). All the T profiles presented in this paper were measured several months after drilling operations. However, the thermal equilibrium might not have been reached as the equilibrium temperature from geothermometer appears hotter. Locally, the vertical profiles are disturbed by T anomalies that match in depth producing fracture and fault zones (FZ) (Figure 1d). This thermal signature of the permeable FZ was already described in the literature [36–40]. The permeable FZs are mainly localized in dacitic tuffs.

This study focused on two deep wells:

- CP-4A, drilled outside the graben, where isotherms suddenly decrease, traducing cooler temperatures;
- CP-6A, drilled inside the graben in the hot core of the reservoir (Figure 1b,c).

This selection was made to identify which factor can influence the permeability, such as temperature, fracture distribution, F/R ratio, lithology, etc.

Even if the CP-4A well, drilled down to 2700 m MD, is in the peripheral limit of the system, a good hydraulic connection to the main reservoir was evident [34]. The deep temperature reached approx. 235 °C and a large negative T anomaly was observed from 2525 to 2650 m MD (Figure 1d). The 3D structural model indicated a fracture zone intersected at 2600 m MD that is potentially permeable as it correlates the T anomaly. This FZ probably controls the hydraulic behavior of the well that presents a high injectivity with an absorption of 310 m³/h without wellhead pressure. The well was sampled from 1540 to 2700 m MD and intersects mainly dacitic tuffs with andesitic lavas interlayered in this section.

The CP-6A well, drilled down to 2300 m MD, mainly intersects dacitic tuffs and andesitic lavas. Cuttings were not available below 1430 m MD due to total losses and, thus, its geological study focused from 360 to 1430 m MD. The deep temperature reached approx. 230 °C, but as temperature profiles were acquired only few months after drilling operations, temperature can be expected to be hotter once the thermal equilibrium reaches that suggested by its twin well CP-6. In CP-6A, there was a double T anomaly: a positive one from 1210 to 1290 m MD matched a first FZ at 1240 m MD and a negative one from 1290 to 1360 m MD matched a second FZ at 1320 m MD from the structural 3D model (Figure 1d). Because they matched a T anomaly, these two FZs were interpreted as permeable, and a

constricted sampling was made around them to observe the possible clay signature of the permeable FZ more accurately in the CP reservoir. The structural model indicated at least three others deep FZs intersected by the well. The deepest one was interpreted as a local fault intersected at 2200 m MD. The CP-6A well presented the highest injectivity index of the geothermal system with 20 m³/h/bar.

3. Sampling and Methods

Petrographic investigations were carried out with 7 thin sections from CP-4A and 11 thin sections from CP-6A observed under polarized microscope and JEOL JSM-IT500 scanning electron microscopy (SEM) at the IC2MP laboratory (University of Poitiers, Poitiers, France). Cuttings with an average size between 0.5 and 2 mm were sampled. With cutting samples, spatial resolution is low and textural relations between minerals are hardly observed.

X-ray diffraction (XRD) was conducted on the clay fraction of 35 samples of cuttings from 1540 to 2700 m MD in CP-4A and 72 samples from 360 to 1430 m MD in CP-6A. The sampling was performed along the reservoir and constricted around the temperature anomalies related to the permeable FZ. Samples far from permeable zones were also selected as reference materials, as they are believed to be representative of rocks preserved from present-day fluid circulation. In the absence of preliminary grinding, samples were immersed in distilled water and disaggregated by ultrasonic treatment to properly disperse the clay particles in suspension. Oriented powders on glass slides were prepared with a <5 µm clay suspension, obtained by sedimentation. Clay minerals were identified by XRD of air-dried and ethylene-glycol (EG)-saturated oriented powders carried out on a Bruker D8 Advance diffractometer (CuK α radiation, 40 kV, 40 mA) at the IC2MP laboratory (University of Poitiers, Poitiers, France). The analytical conditions were as follows: angular domain: 2.5–30 °2 θ ; step increment: 0.025 °2 θ ; and counting time per step: 3 s. Diffractometers were processed using Match! Software (Version 3.8, Crystal Impact) and clay minerals were identified according to [41].

Chemical compositions of primary and secondary minerals as well as textural observations were acquired using a JEOL JSM-IT500 SEM equipped with a Bruker linxeye EDS associated with SPIRIT software (Version 2.1, Bruker, Billerica, MA, USA) at the IC2MP laboratory (University of Poitiers, Poitiers, France). The analytical conditions were as follows: 15 kV; 1 nA; counting time: 50 s; and working distance: 11 mm. The analyzed elements were Si, Al, Fe, Mg, Mn, Ti, Ca, Na, and K. The system was calibrated with a variety of synthetic oxide and natural silicate standards. The reproducibility of the standard analyses was approximately 1%, except for Na, which had a reproducibility of 1.5%.

4. Results

4.1. Alteration Petrography

The former petrography described by [24] was slightly modified in the light of our observations. In this sense, samples CP-4A 1640, 1790, and 1940 presented orthopyroxenes suggesting a more andesitic lava flow. Samples CP-4A 2340 and CP-6A 860 were cuttings from andesitic to dacitic rocks, suggesting that they were at the transition between andesitic lavas and dacitic formations.

A pervasive alteration was observed in all samples with a moderate to intense intensity. This alteration pattern was particularly well-expressed away from zones of circulation. Smectite was observed as the replacement of orthopyroxenes in the andesitic lavas (Figure 2a). In shallow samples (above 800 m MD), smectite was associated with zeolites, hematite, and carbonates (calcite and ankerite).

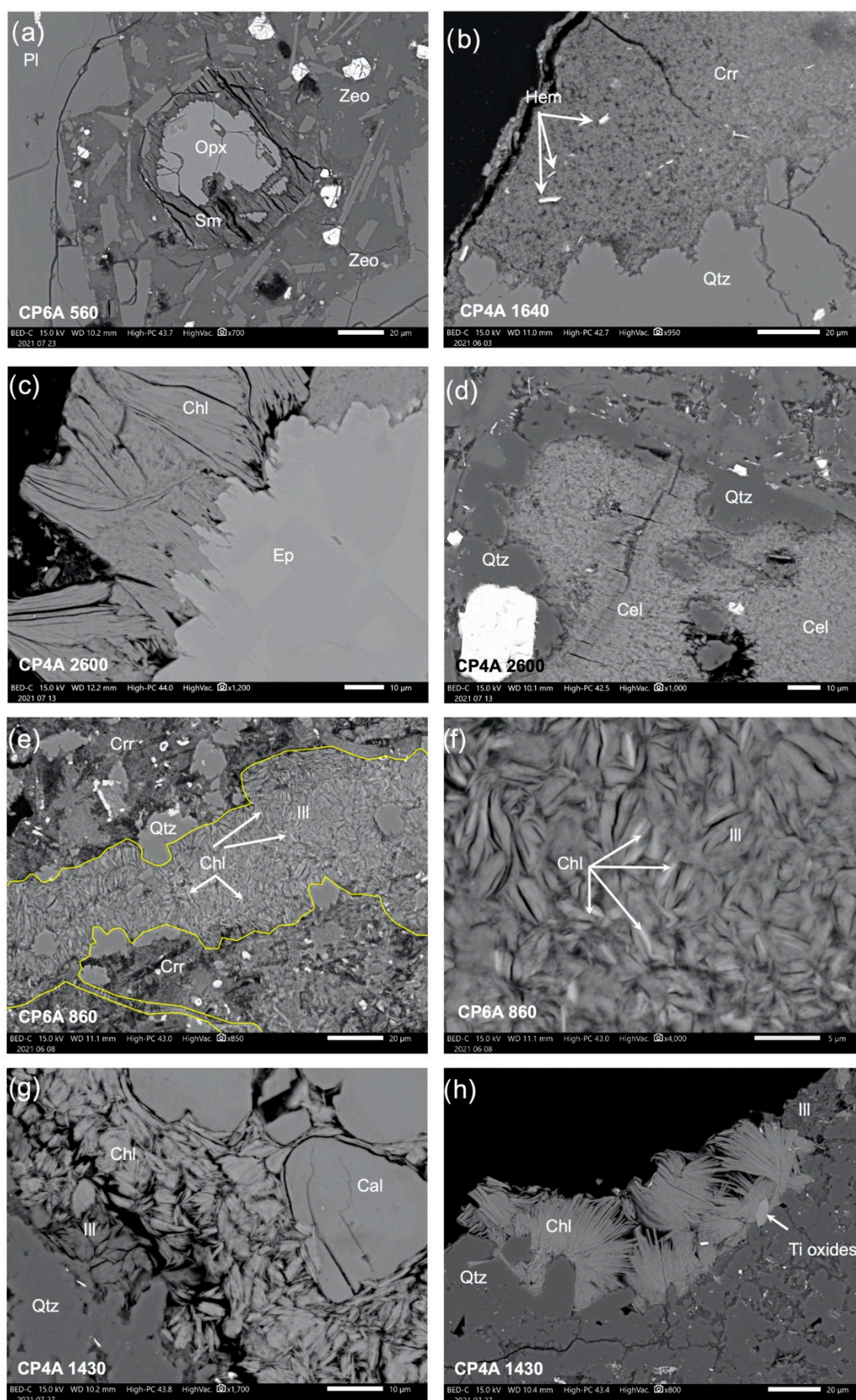


Figure 2. Mineral associations representative of pervasive alteration (a–d) and fracture-controlled alteration (e–h). Observations conducted by SEM in thin sections of cuttings fixed in epoxy in CP-4A and CP-6A wells. Cal: calcite, Chl: chlorite, Cpt: clinoptilolite, Crr: corrensite, Ep: epidote, Hem: hematite, Ill: illite, Opx: orthopyroxen, Pl: plagioclase, Sm: smectite, Qtz: quartz, Zeo: zeolite.

In CP-6A, zeolites with a reflection peak at 8.95–8.96 Å in the oriented XRD corresponded to the heulandite-clinoptilolite group (Figure 3). However, chemical analyses were closer to heulandite (Table S1 Supplementary Materials). Chloritic minerals mainly replaced magmatic ferromagnesian minerals and the vitreous matrix (Figure 2b). In deep samples below 1500 m MD, especially in CP-4A, chloritic minerals were observed in association with titanite and epidote (Figure 2c). Sometimes epidote precipitates in small needle-shaped crystals inside chlorite. Epidote is iron-rich with $P_s > 0.30$ and exhibited chemical heterogeneity evidence in zonation observed under SEM back-scattered electrons (Figure 2c and Table S2). Green minerals were observed in all the shallow as well as deep samples associated with quartz micrograins as microvacuoles, vesicles and vug fillings as well as in total replacement of the magmatic minerals. They are Fe,K-rich clays from the celadonite–glaucanite group (Figure 2d). Chemical analyses showed that celadonite occurred in the deepest sample at 2600 m MD in CP-4A, whereas in the shallowest samples at 560 and 980 m MD in CP-6A, the high tetrahedron charge indicated minerals closer to glaucanite (Table S3) [42,43].

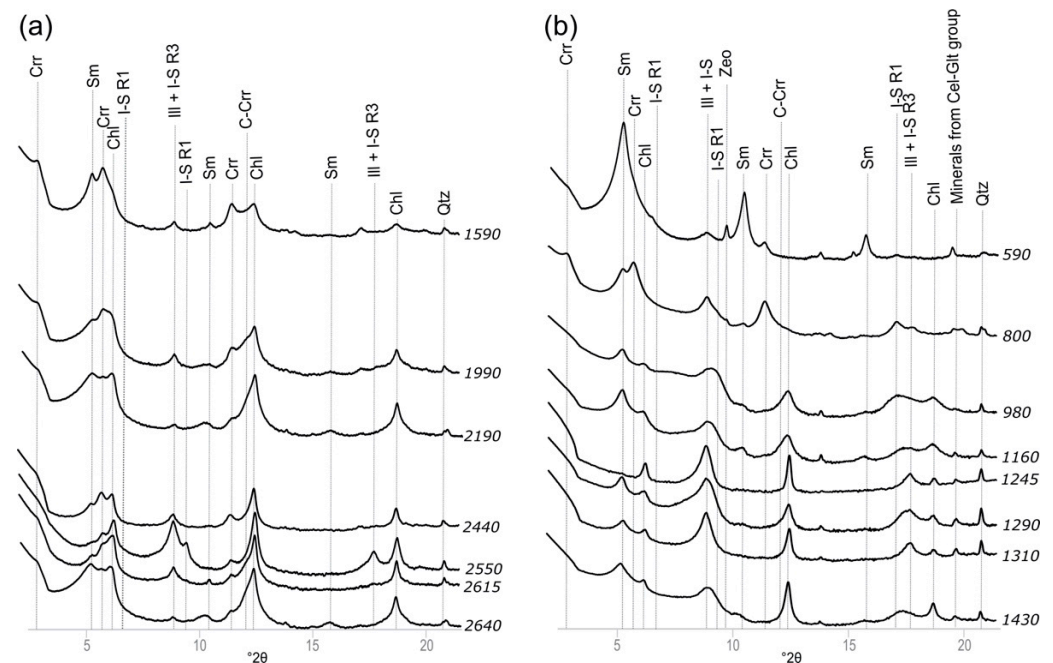


Figure 3. X-ray diffractograms of EG-saturated oriented powder (<5 μm clay fraction). (a) Samples 1590, 1990, 2190, 2440, 2550, 2615, and 2640 in CP-4A well. Samples 2550 and 2615 were located inside the FZ associated with negative T anomaly. (b) Samples 590, 800, 980, 1160, 1245 (upper FZ associated with positive T anomaly), 1290, 1310 (lower FZ associated with negative T anomaly), and 1430 in CP-6A well. Cel: celadonite, Chl: chlorite, C-Crr: chlorite–corrensite mixed layers, Crr: corrensite, Glt: glaucanite, Ill: illite, I-S: illite–smectite mixed layers, Sm: smectite, Qtz: quartz, Zeo: zeolites.

A fracture-controlled alteration event was superimposed on the previous pervasive alteration (Figure 2e). It was very destructive and the primary minerals or the secondary minerals from the pervasive alteration were strongly replaced in the zones of fluid circulation at 2600 m MD in CP-4A and 1240 and 1320 m MD in CP-6A. It was characterized by illitic minerals that seemed to precipitate together with chlorite +/– carbonates, mainly calcite but also sometimes dolomite (Figure 2f,g). Coprecipitation of illite and chlorite suggests the occurrence of at least one other generation of chlorite than the one observed previously in association with epidote and titanite (Figure 2c,e–h).

4.2. Depth-Related Distribution of Clay Minerals

The relative proportions of the clay minerals observed were also estimated from peak areas in the XRD patterns (Figure 3). The higher the area of the peak, the most abundant that clay mineral. When mixed layers such as I-S and/or C-Crr were identified after EG-saturation, the complex peaks were deconvoluted in Gaussian curves using the Fityk software. This deconvolution was made in the 7–11 °2θ domain for the illitic minerals (Figure 4a). The illitic peak was decomposed with at least two peaks related to I-S R3; the first one with d-spacing around 10.1–11.4 Å and a second one, more intense, with d-spacing around 9.55–10 Å. Sometimes, a third peak of pure illite was added at 10 Å to the decomposition. Due to a very low intensity of the reflection patterns, it was not possible to apply the deconvolution of the chloritic peak on the 16–21 °2θ domain as proposed by [44] for all the samples and, thus, was mainly performed on the 10–14 °2θ domain (Figure 4b,c). After deconvolution of the 10–14 °2θ domain in EG patterns, the corrensite peak was between 7.63 and 7.85 Å, the C-Crr one was between 7 and 7.9 Å, and the chlorite one between 7.07 and 7.12 Å (Figure 4b). For chloritic minerals in the CP-4A well, the relative proportion was defined as $\%Chl = \text{area Chl} / (\text{area Chl} + \text{area C-Crr} + \text{area Crr})$ after deconvolution of the peaks (Figure 5).

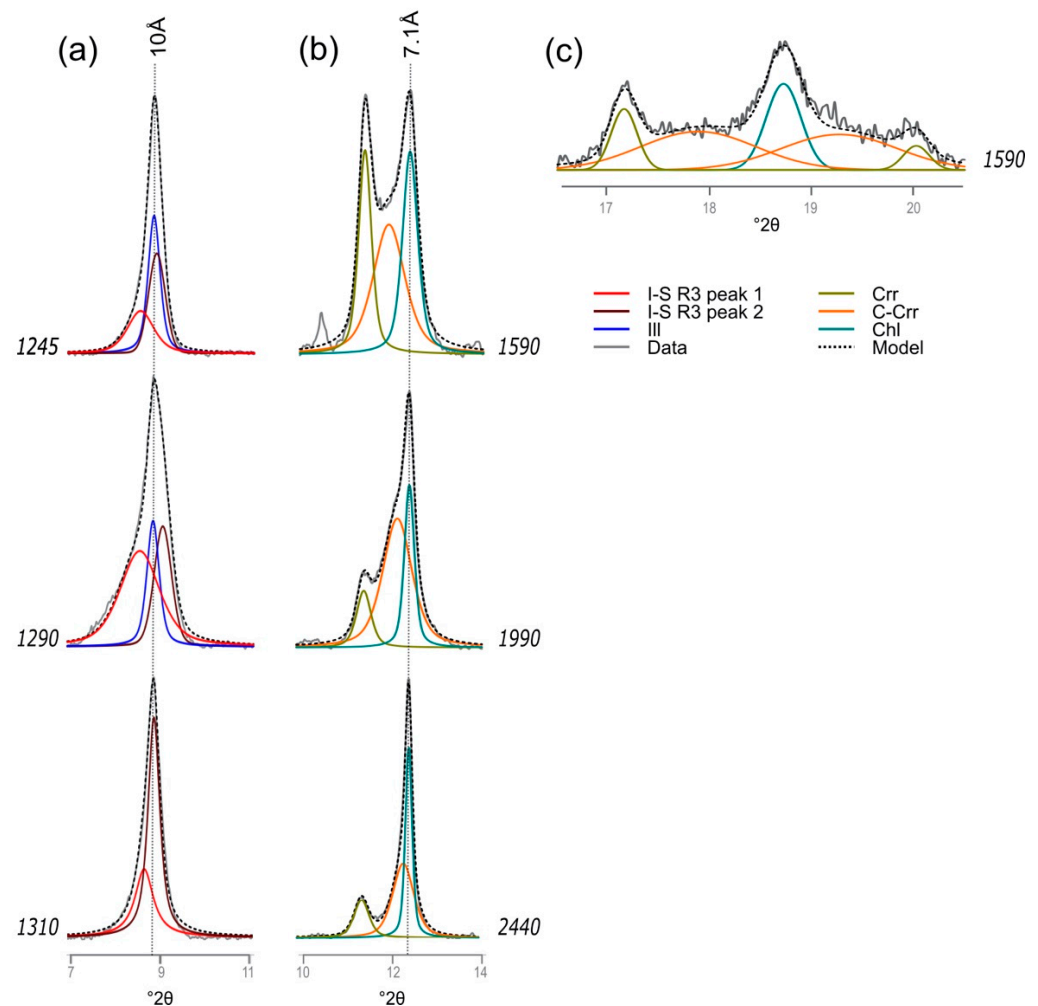


Figure 4. Deconvolution of the X-ray diffractograms of EG-saturated oriented powder (<5 μm clay fraction). (a) Illitic peak (7–11 °2θ domain) of the samples CP-6A 1245 (upper FZ associated with positive T anomaly), 1290 (edges of FZ), and 1310 (lower FZ associated with negative T anomaly).

Ill: illite, I-S: ordered illite/smectite mixed layer. (b) Deconvolution of the chloritic peak (10–14°2θ domain) of the samples CP-4A 1590 (corrensite dominant), 1990 (C-Crr dominant), and 2440 (chlorite dominant). Chl: chlorite, Crr: corrensite, C-Crrl: chlorite–corrensite mixed layer. (c) Deconvolution of the chloritic peak (16–21 °2θ domain) of the sample CP-4A 1590.

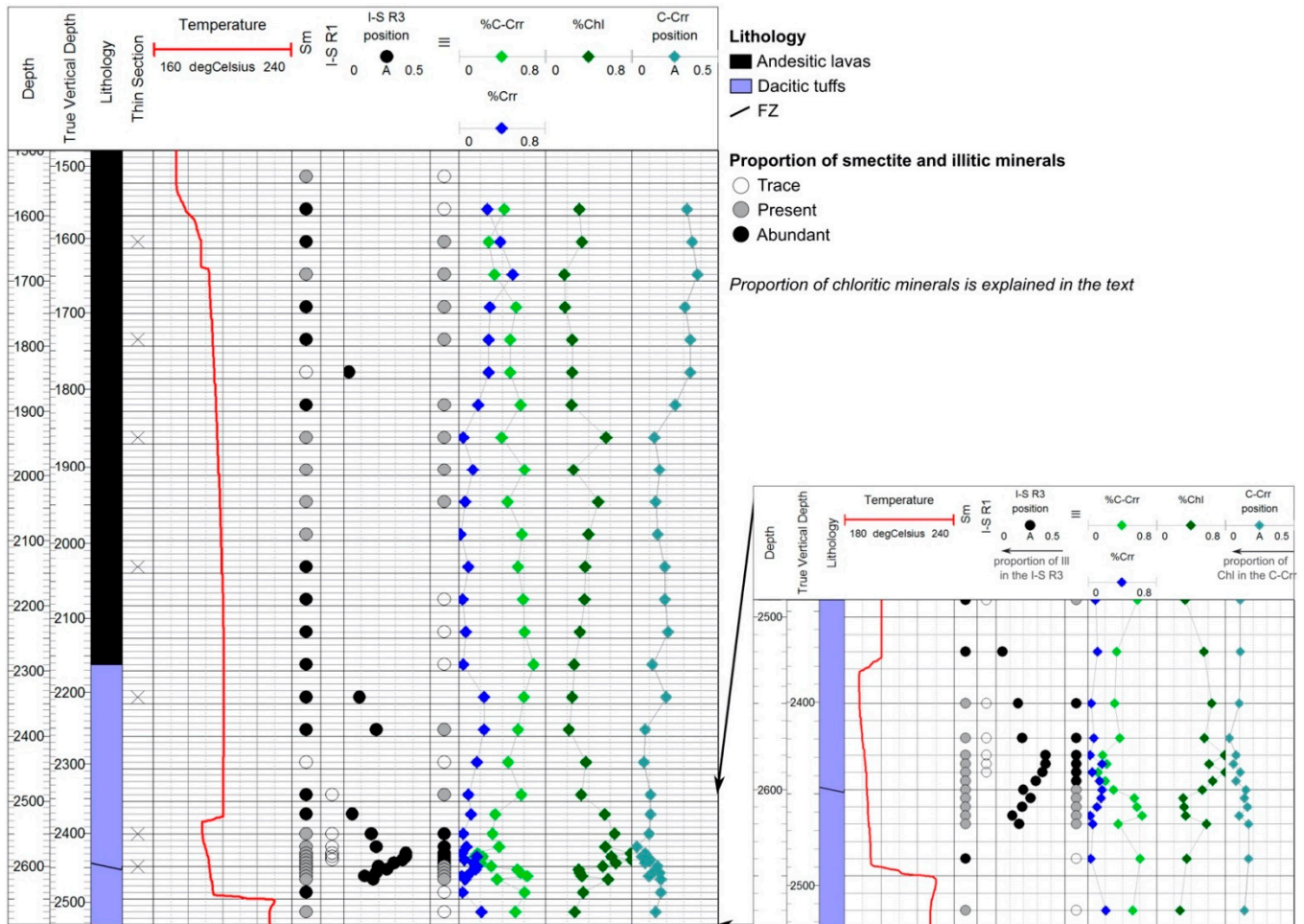


Figure 5. Relative proportion of clay mineral with depth estimated from EG-saturated XRD patterns within the CP-4A well with a close-up of the FZ shown on the right. The temperature profile was measured 2 ½ months after drilling operations. Depth is expressed in m (measured depth). I-S R3 and C-Crr positions are expressed in Ångstrom. Sm: smectite, I-S: illite/smectite mixed layers, Ill: illite, C-Crr: chlorite/corrensite mixed layers, Crr: corrensite, Chl: chlorite.

The proportion of illite in the I-S was estimated thanks to the position of peak 2 after deconvolution; the closer the peak is from the theoretical position of illite (10 Å), the higher the proportion of illite inside the I-S (Figure 4a). In Figures 5 and 6, the *I-S R3 position* is the difference between the position of the peak 2 after deconvolution and the theoretical position of illite (10 Å). As the *I-S R3 position* was comprised between 0.03 and 0.36 Å, the proportion of illite inside the I-S R3 was estimated between 100% and 90% [45].

The proportion of chlorite in the C-Crr was estimated thanks to the position of the C-Crr peak; the closer the peak is from the theoretical position of chlorite (7.1 Å), the higher the proportion of chlorite inside the C-Crr. In Figures 5 and 6, the *C-Crr position* is the difference between the position of the C-Crr peak after deconvolution and the theoretical position of chlorite (7.1 Å), comprised between 0.03 and 0.46 Å.

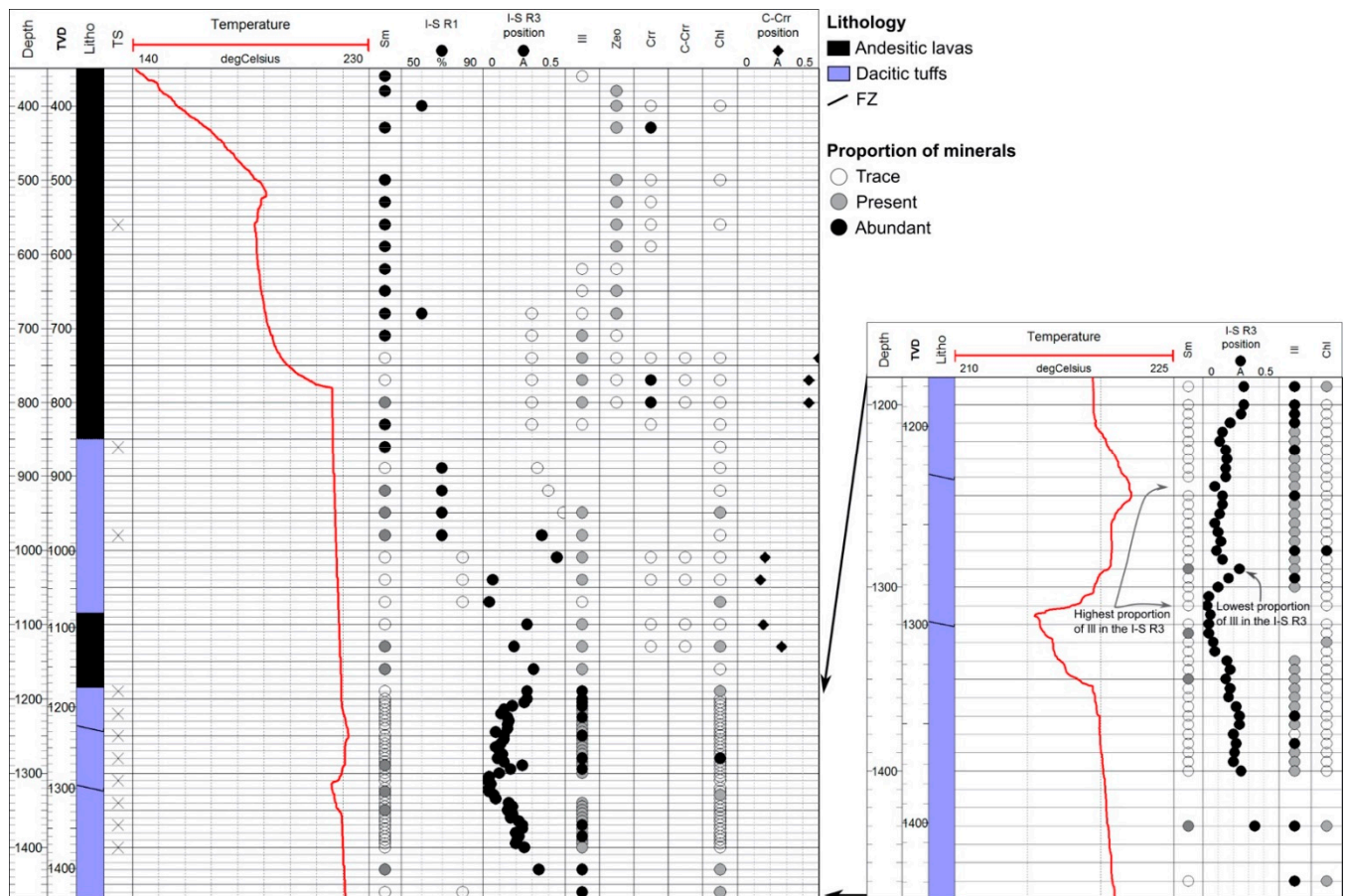


Figure 6. Relative proportion of clay mineral with depth estimated from EG-saturated XRD patterns within CP6A well with a close-up of the FZ shown on the right. The temperature profile was measured 4 months after drilling operations. I-S R3 and C-Crr positions are expressed in Ångstrom. I-S R1 are expressed in percentage of illite comprised between 60 and 80%. Depth: Measured Depth (m), TVD: True Vertical Depth, Litho: Lithology, TS: Thin Section, Sm: smectite, I-S: illite/smectite mixed layers, Ill: illite, C-Crr: chlorite/corrensite mixed layers, Crr: corrensite, Chl: chlorite.

4.2.1. Trioctahedral Clays Related to Pervasive Alteration

The trioctahedral sequence (Sm-Crr-C-Crr-Chl) was clearly visible in CP-4A (Figure 3a). The smectite was identified with a high reflection peak between 16.7 and 17.3 Å and a lower intensity of other reflection peaks in EG patterns (Figure 3a). The proportion of chloritic minerals increased with depth and temperature (Figure 5). The relative proportion of corrensite gradually decreased with depth when the C-Crr increased. Corrensite barely disappeared in the deepest part of the well where chlorite was more abundant, especially inside the FZ. Below 1900 m MD, the C-Crr peak shifted towards the chlorite position (7.1 Å), traducing an increase in the chloritic component at the expense of the corrensite one in the C-Crr (Figure 5). The trioctahedral sequence was obliterated from 2530 to 2620 m MD, the zone of circulation, but was dominating again below 2620 m MD.

This trioctahedral sequence was also visible in CP-6A, especially above 880 m MD, far from the permeable FZs (Figures 3 and 6). Inside the permeable FZs, the trioctahedral clays were obliterated by dioctahedral ones. In these samples, pure chlorite (without corrensite and C-Crr) was still observed in trace amounts.

4.2.2. Dioctahedral Clays Related to Fracture-Controlled Alteration

The dioctahedral sequence (I-S R1–I-S R3–Ill) was clearly visible below 890 m MD in CP-6A (Figure 3b). With increasing depth and temperature, the dioctahedral sequence from I/S Ri to I/S R3 to pure illite (without I-S detected) was clearly observed below 890 m

MD. Transition from I-S R1 rich in smectite (60 to 80%) to I-S R3 rich in illite (>90%) was observed around 980 m MD and the pure illite was abundant below 1190 m MD (Figure 6). Locally, the percentage of illite in the I-S R3 increased slowly in the vicinity of both FZs with a maximum illitic component at 1245 and 1310 m MD, whereas the minimum was observed at 1290 m MD in between both FZs (Figure 4a). Pure illite disappeared at the depth of the lower FZs (associated to the negative T anomaly) and reappeared again below 1340 m MD (Figures 4a and 6).

Diocahedral clays (illite and I-S R3 with illite >90%) also dominated the permeable FZ associated with the T anomaly from 2530 to 2620 m MD in the CP-4A well (Figure 3a). Inside the FZ, I-S R1 and R3 and abundant pure illite were observed above 2600 m MD, the depth of the fracture. Below 2600 m depth, the amount of I-S R3 and pure illite decreased, whereas R1 was no longer observed. Inside the I-S R3, the highest percentage of illite was observed in the vicinity of the fracture, and the illitic component decreased far from the fracture (Figure 5).

4.3. Crystal Chemistry of Clay Minerals

The average structural formulas of smectite observed in samples CP6A 560 & 860 are given in Table S4. All the smectites were trioctahedral, i.e., saponite, with XFe ratios ($\text{Fe}/(\text{Fe} + \text{Mg})$) between 0.2 and 0.5, probably relative to the chemistry of the mineral that they were replacing (Figure 7a).

The average structural formulas of corrensite observed in samples CP-4A 1640 and 2340 and CP-6A 560 are provided in Tables S4 and S5. The interlayer charge was between 0.23 and 0.49, an octahedral occupancy between 5.10 and 5.57 a.p.f.u., and a Si/(Si + Al) ratio >0.6.

The average structural formulas of C-Crr observed in samples CP-4A 1790, 1940, 2140, and 2550 are provided in Table S5. They presented a lower interlayer charge than the pure corrensite (without C-Crr detected) and a higher octahedral occupancy. The enrichment of Fe suggested an increase in the chloritic layers in the mineral that tended to increase with depth as was also observed with the XRD patterns (Figure 7a).

The average structural formulas of chlorite observed in samples CP-4A 2340, 2550, and 2600, and CP-6A 860, 980, 1190, 1220, 1250, 1310, 1370, 1400, and 1430 are provided in Tables S4 and S5. They differed from the corrensite by a lower interlayer charge (between 0.01 and 0.3 a.p.f.u.), a higher octahedral occupancy (>5.70), and by a lower Si/(Si + Al) ratio (<0.60). Two types of chlorite were distinguished based on XFe ratio (Figure 1). The Fe-Mg chlorite with $0.2 < \text{XFe} < 0.5$ were observed in association with corrensite and C-Crr in replacement of all ferromagnesian magmatic minerals. These chloritic minerals are related to the pervasive alteration. The Fe-chlorite with $0.55 < \text{XFe} < 0.80$ precipitate mainly with illitic minerals in veins. Sometimes, they were observed in replacement of Fe-Mg chlorite and corrensite from the pervasive alteration as in sample CP-4A 2340 in Figure 1b. This second generation of Fe-chlorite is related to the argillic alteration developed in the FZ. When they coprecipitated with illitic minerals, the interlayer charge was slightly higher due to contamination. Some measurements of chlorite are in between both.

The chemical analyses of illitic minerals (I-S R1, I-S R3, and illite) did not present major variations with depth and in both wells (Table S6). The interlayer charge was between 0.70 and 0.90 for I-S and higher than 0.90 for pure illite.

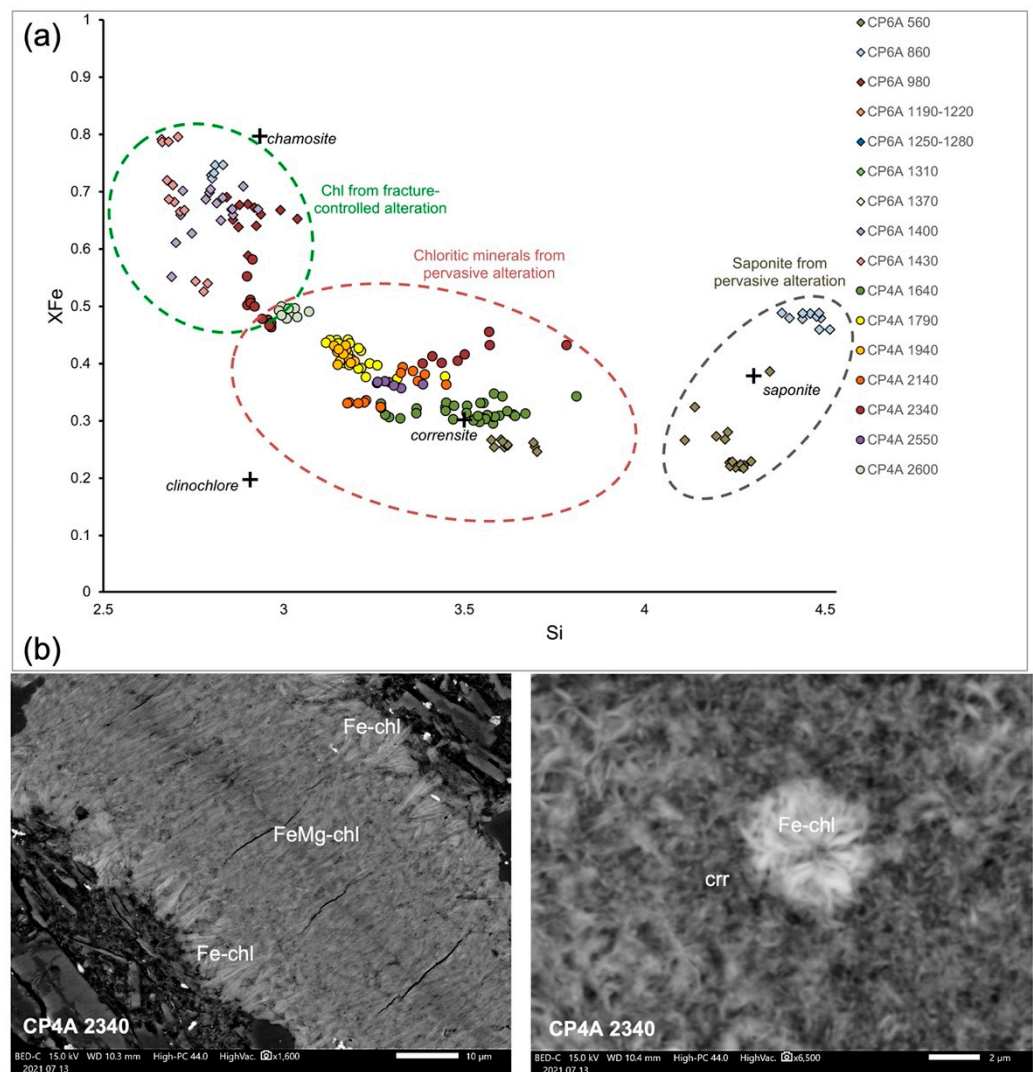


Figure 7. (a) Plot of the structural formulae of trioctahedral clays in a diagram of XFe versus Si for CP-4A and CP-6A wells ($X_{Fe} = Fe/(Fe + Mg)$). The average structural formula for each sample is presented in S1. In this figure, all the samples are represented with a relative structure containing 14 oxygen atoms and assuming that the total iron content was composed of Fe^{2+} . Theoretical compositions of clinochlore, chamosite, corrensite, and saponite are provided for reference. (b) SEM observations of Fe-chlorite from the fracture-controlled alteration superimposed to the Fe-Mg chlorite and corrensite from the pervasive alteration.

5. Discussion

5.1. Clay Signature of the Hydrothermal Alteration

Petrographic observations suggested at least two hydrothermal alterations:

A pervasive alteration associated with two mineralogical assemblages:

- *Saponite + heulandite–clinoptilolite ± hematite ± carbonates (calcite + ankerite)* observed as the replacement of primary minerals as well as of the vitreous matrix in the shallowest samples. Heulandite–clinoptilolite showed thermal stability up to 200 °C [46,47].
- *Corrensite–Fe-Mg chlorite + epidote + titanite + quartz + hematite* observed as the replacement of primary minerals as well as of the vitreous matrix in the deepest samples of the reservoir.

This propylitic alteration is very common during cooling of magmatic intrusive bodies resulting from interactions between igneous minerals with stagnant fluids in pores or microcracks [48,49]. In the context of the andesitic volcanism, it is mainly dominated

by trioctahedral clays and is representative of hydrothermal alteration in inactive flow regimes [8]. More locally, green Fe,K-rich clays from celadonite–glaucanite group + quartz were observed as the replacement of primary minerals as well as filling open spaces such as microvacuoles, microfractures, and vesicles in the reservoir. These green Fe,K-rich clays are poorly characterized by the literature and could result from late hydrothermal fluids. The occurrence of minerals such as celadonite, iron-rich epidote, and hematite in which iron is essentially in the ferric state is indicative of crystallization in oxidizing conditions. The chemistry of chloritic minerals is rock-dominated during propylitic alteration and they are preferentially magnesium-rich (i.e., $Fe/Fe + Mg < 0.5$) because they incorporate iron essentially at the ferrous state under oxidizing conditions [50–52].

A fracture-controlled alteration marked by *illite + I-S + Fe-chlorite + carbonates (mainly calcite)*. This alteration was superimposed on the previous one and was particularly intense in the proximity of fractures. This mineral's assemblage was widely developed in zones of active flow regime structurally controlled by fracture networks at $200\text{ }^{\circ}\text{C} < T < 300\text{ }^{\circ}\text{C}$ [8,48]. With our study, we can hypothesize that this hydrothermal association is probably the alteration signature of present-day circulations of the reservoir geothermal fluids within the CP geothermal system. In the future, it could be interesting to study the chemical equilibrium of the dioctahedral clays with the geothermal fluid at the downhole measured temperatures to confirm this assumption. Minerals precipitate directly from the fluid and their chemistry is controlled by the fluid's [19,52,53]. Contrary to the chlorite from the propylitic event, chlorites from the argillic event crystallized under reducing conditions and are Fe-rich. Carbonates suggest a relatively high CO_2 content in the geothermal fluid. In this sense, the steam fraction was not analyzed in CP-6, but in the nearby wells, the CO_2 content comprised between 2.18 and 3.5 mmol/mol [33].

All these minerals can crystallize in the present-day temperature observed in the wells (circa $250\text{ }^{\circ}\text{C}$). The propylitic alteration probably started before but continues even if, locally in the permeable levels, hydrothermal minerals that crystallized directly from the fluid obliterate the propylitic minerals.

5.2. Towards a Conceptual Model of the Deep Fluid Circulations

The interpretation of the propylitic alteration associated with the active part of the reservoir and fracture distribution proposed by [6,34] is too simplistic. Our results revealed a high heterogeneity in terms of alteration mineralogy that underlines the dynamics of the fluid. The CP-6A well, located inside the graben, in the hot core of the reservoir, was dominated by the dioctahedral sequence with a relative proportion of illitic component that increased in the vicinity of the FZs (Figure 8a). The CP-4A well, located at the peripheral limit of the geothermal system, was dominated by the trioctahedral sequence, from saponite to chlorite, including corrensite and C-Crr, influenced by the regional geothermal gradient (Figure 8a). However, the same intense illitization was observed in the deep permeable FZ of the well. Although no discharge fluid samples have been analyzed yet for the CP-4A well, the similarity in alteration mineral assemblages and chemical homogeneity of the clay minerals supports the theory of a common fluid source and suggests that the graben fault can behave as a conduit for the geothermal fluid (Figure 8b). The proximity of both wells to each other (circa 2 km between the bottoms of the wells) and the injectivity index of CP-4A confirms a good connection to the deep geothermal reservoir. However, the sudden decrease in the isotherms and the dominance of propylitic alteration in CP-4A suggests limited fluid circulations outside the graben restricted to a few FZs compared to the center of the graben.

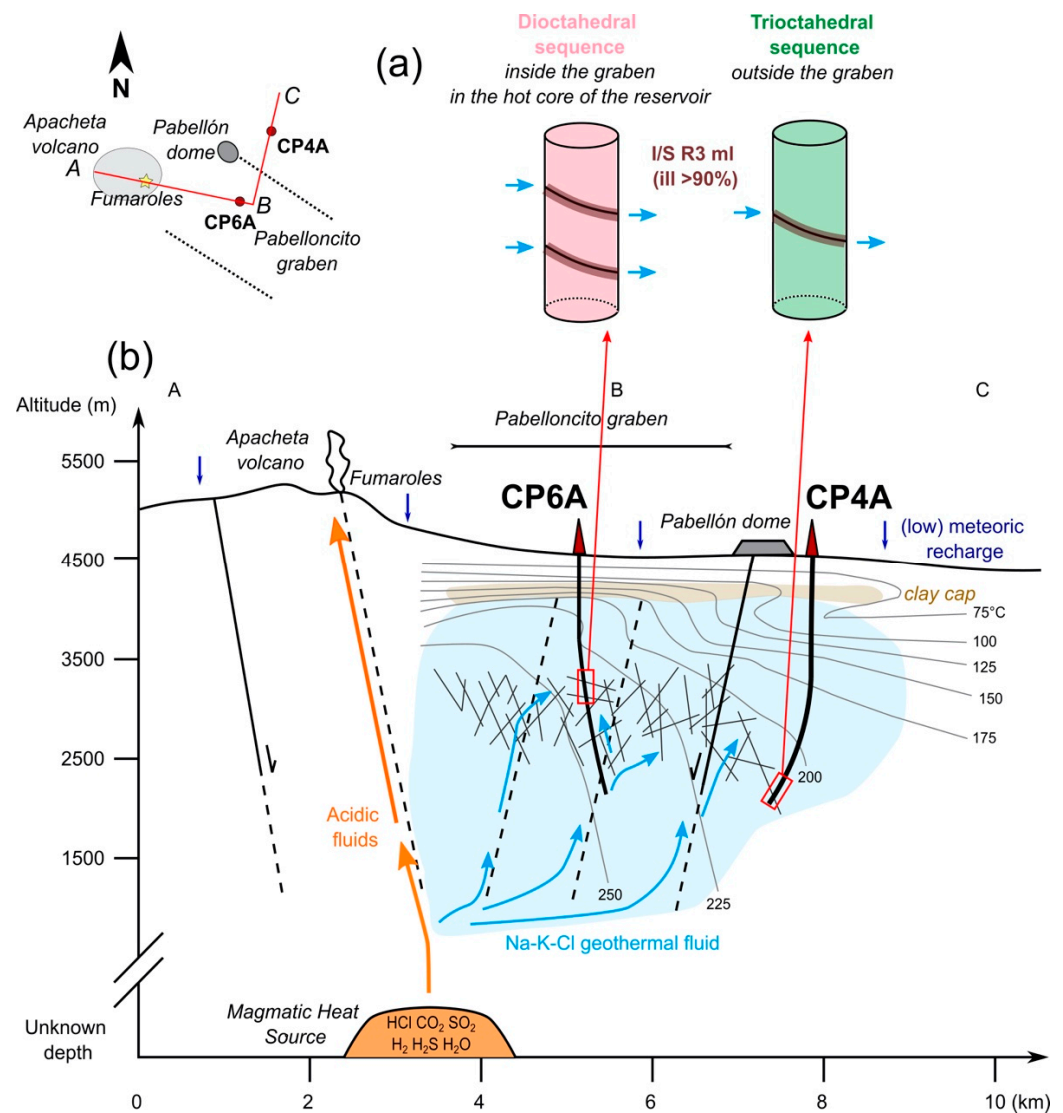


Figure 8. (a) Clay signature of the deep fluid circulations in Cerro Pabellón (CP) wells. (b) Conceptual model of the CP geothermal system after [4,6,7,33]. Isotherms, structures, and fluid circulations are schematically represented and updated with our results in the CP-4A and CP-6A wells. The large-scale faults are from the structural model of [24] and the fractured core of the reservoir follows the trace of the low resistive anomaly in the 3D magnetotelluric model from [34]. The depth of the magmatic heat source is from [54].

Deep and hot geothermal fluid (>250 °C) ascends through a widely distributed fracture system connected to highly dipping NW-striking normal faults. The degassing processes and intense leaching of the host volcanic rocks that probably occurs at depth lead to an increase in solutes in the geothermal fluid [32,33]. In a high F/R ratio environment such as a permeable fracture, geothermal fluid becomes strongly oversaturated in K, promoting the crystallization of illitic minerals. Illitic minerals are widely described in the literature as potential indicators of actual circulations [52,55,56]. At the FZ scale, I-S R3 (illite > 90%) was observed at the depth of the main drains, whereas illite was more abundant in the altered walls of the fracture (above the drain for CP-4A and on both sides of the drains for CP-6A). These local variations could be linked to local variations in the physico-chemical conditions in FZs. Indeed, abrupt changes in the flow regime inside the fluid channels can lead to the explosive nucleation of small clay crystallites and promote the occurrence of heterogeneous mineral assemblages, such as I-S. This conceptual model of circulations should be consolidated by alteration studies in other wells of the geothermal system but

also integration of the chemical composition of its fluids. If fracture distribution and fluid dynamics seem to be dominant factors of the alteration, observations in other wells of the field could also help to understand the influence of the graben fault or geomechanics of the host rocks.

6. Conclusions

As the CP reservoir is an active system, it presents a high heterogeneity in terms of alteration mineralogy. At least two main stages of hydrothermal alteration were identified in the CP-4A and CP-6A wells. A pervasive alteration, dominated by trioctahedral clays and calcosilicates, was observed far from the permeable FZ in replacement of primary minerals. It was an intense fracture-controlled event dominated by illitic minerals (I-S R3 with ill > 90% and illite), Fe-chlorite, and calcite that crystallized directly from fluid in the FZs. This alteration is superimposed on the previous one and can be highly destructive.

Pervasive and fracture-controlled alterations could occur synchronously, but, locally, the fluid dynamics led to replacement of the minerals from propylitic alteration. The dioctahedral sequence was mainly expressed in CP-6A, in the hot core of the reservoir inside the graben, where the fluid circulations are more intense, whereas the trioctahedral sequence was mainly expressed in CP-4A, outside the graben. However, in both wells, the FZs that channel the ascending fluid were associated with a strong illitization. This specific clay signature observed in high F/R ratio environment is a good indicator of present-day fluid circulations, suggesting one unique fluid circulating and the permeable behavior of the graben fault.

These first original results from the deep mineralogy in CP-4A and CP-6A provide the opportunity to understand deep circulations in the CP geothermal system and are very helpful for interpreting the active zone and present-day productivity of the reservoir. Moreover, they underline the importance of studying clay minerals for geothermal prospections for the future evolution of the CP but also for other Andean geothermal systems.

Supplementary Materials: The following supporting information can be downloaded at: <https://www.mdpi.com/article/10.3390/min12101244/s1>, Table S1. Calculation of structural formula of zeolites at 560 m depth in CP-6A well, Table S2. Calculation of structural formula of epidote at various depths in CP-4A well, Table S3. Calculations of structural formulae of green Fe,K-rich clays from celadonite–glauconite group at various depths in CP-4A and CP-6A wells [57], Table S4. Calculations of structural formulae of trioctahedral clays at various depths in CP-6A wells, Table S5. Calculations of structural formulae of trioctahedral clays at various depths in CP-4A wells, Table S6. Calculations of structural formulae of some illitic minerals at various depths in CP-4A and CP-6A wells.

Author Contributions: Conceptualization, J.V. and D.M.; resources, G.R. and G.V.; investigation, J.V., P.P., D.B. and S.M.; writing—original draft preparation—review and editing, J.V.; funding acquisition, J.V. and D.M. All authors have read and agreed to the published version of the manuscript.

Funding: This study benefited from the scientific and financial support of the Andean Geothermal Center of Excellence (CEGA), Anid-Fondap projects #15090013, 15200001, and ACE210005. This study was published in the framework of the Anid-Fondecyt postdoctoral grant n° 3210150 of J. Vidal.

Data Availability Statement: Not applicable.

Acknowledgments: Our thanks to Geotérmica del Norte (GDN) for authorizing the use of well data from the Cerro Pabellón project. The authors would like to kindly thank the four anonymous reviewers for their constructive remarks.

Conflicts of Interest: The authors declare no conflict of interest.

Abbreviations

CAVZ: Central Andean Volcanic Zone, CP: Cerro Pabellón, MD: measured depth, I-S: illite–smectite mixed layers, C-Crr: chlorite–corrensite mixed layers, FZ: fracture and fault zone, T: temperature, SEM: scanning electron microscopy, XRD: X-ray diffraction.

References

1. Aravena, D.; Muñoz, M.; Morata, D.; Lahsen, A.; Parada, M.Á.; Dobson, P. Assessment of High Enthalpy Geothermal Resources and Promising Areas of Chile. *Geothermics* **2016**, *59*, 1–13. [CrossRef]
2. Stern, C. Active Andean Volcanism: Its Geologic and Tectonic Setting. *Rev. Geol. Chile* **2004**, *31*, 161–206. [CrossRef]
3. Procesi, M. Geothermal Potential Evaluation for Northern Chile and Suggestions for New Energy Plans. *Energies* **2014**, *7*, 5444–5459. [CrossRef]
4. Urzúa, L.; Powell, T.; Cumming, W.B.; Dobson, P. Apacheta, a New Geothermal Prospect in Northern Chile. *Trans. Geotherm. Resour. Counc.* **2002**, *26*, 65–69.
5. Cappetti, G.; Giorgi, N.; Arias, A.; Volpi, G.; Rivera, G.; Cei, M.; Fedeli, M.; Di Marzio, G.; Pasti, M.; Massei, S.; et al. The Cerro Pabellón Geothermal Project (Chile): From Surface Exploration to Energy Production. In Proceedings of the World Geothermal Congress 2020+1, Reykjavik, Iceland, 24–27 October 2021.
6. Maza, S.N.; Collo, G.; Morata, D.; Lizana, C.; Camus, E.; Taussi, M.; Renzulli, A.; Mattioli, M.; Godoy, B.; Alvear, B.; et al. Clay Mineral Associations in the Clay Cap from the Cerro Pabellón Blind Geothermal System, Andean Cordillera, Northern Chile. *Clay Miner.* **2018**, *53*, 117–141. [CrossRef]
7. Taussi, M.; Nisi, B.; Pizarro, M.; Morata, D.; Veloso, E.A.; Volpi, G.; Vaselli, O.; Renzulli, A. Sealing Capacity of Clay-Cap Units above the Cerro Pabellón Hidden Geothermal System (Northern Chile) Derived by Soil CO₂ Flux and Temperature Measurements. *J. Volcanol. Geotherm. Res.* **2019**, *384*, 1–14. [CrossRef]
8. Beaufort, D.; Westercamp, D.; Legendre, O.; Meunier, A. The Fossil Hydrothermal System of Saint Martin, Lesser Antilles: Geology and Lateral Distribution of Alterations. *J. Volcanol. Geotherm. Res.* **1990**, *40*, 219–243. [CrossRef]
9. Reyes, A.G. Petrology of Philippine Geothermal Systems and the Application of Alteration Mineralogy to Their Assessment. *J. Volcanol. Geotherm. Res.* **1990**, *43*, 279–309. [CrossRef]
10. Mas, A.; Patrier, P.; Beaufort, D.; Genter, A. Clay-Mineral Signatures of Fossil and Active Hydrothermal Circulations in the Geothermal System of the Lamentin Plain, Martinique. *J. Volcanol. Geotherm. Res.* **2003**, *124*, 195–218. [CrossRef]
11. Patrier, P.; Bruzac, S.; Pays, R.; Beaufort, D.; Bouchot, V.; Verati, C.; Gadhia, A. Occurrence of K-Feldspar-Bearing Hydrothermal Breccias in the Bouillante Geothermal Field (Basse Terre–Guadeloupe). *Bull. Société Géologique Fr.* **2013**, *184*, 119–128. [CrossRef]
12. Glaas, C.; Vidal, J.; Patrier, P.; Girard, J.-F.; Beaufort, D.; Petit, S.; Genter, A. How Do Secondary Minerals in Granite Help Distinguish Paleo- from Present-Day Permeable Fracture Zones? Joint Interpretation of SWIR Spectroscopy and Geophysical Logs in the Geothermal Wells of Northern Alsace. *Geofluids* **2019**, *2019*, 8231816. Available online: <https://www.hindawi.com/journals/geofluids/2019/8231816/> (accessed on 18 December 2019).
13. Prasetyo, I.; Koestono, H.; Thamrin, H. Clay Alteration Study from Wells of Tompaso Geothermal Field, North Sulawesi, Indonesia. In Proceedings of the World Geothermal Congress 2015, Melbourne, Australia, 19 April 2015.
14. Teklemariam, M.; Battaglia, S.; Gianelli, G.; Ruggieri, G. Hydrothermal Alteration in the Aluto-Langano Geothermal Field, Ethiopia. *Geothermics* **1996**, *25*, 679–702. [CrossRef]
15. Vidal, J.; Patrier, P.; Betancourt, C.; Maza, S.; Morata, D. First Results of the Vein Alteration in the Deep Well PGC1 of Irruputuncu Geothermal System, Andean Cordillera, Northern Chile. In Proceedings of the World Geothermal Congress 2020+1, Reykjavik, Island, 24–27 October 2021.
16. Vásquez, M.; Nieto, F.; Morata, D.; Droguett, B.; Carrillo-Rosua, F.J.; Morales, S. Evolution of Clay Mineral Assemblages in the Tinguiririca Geothermal Field, Andean Cordillera of Central Chile: An XRD and HRTEM-AEM Study. *J. Volcanol. Geotherm. Res.* **2014**, *282*, 43–59. [CrossRef]
17. Flexser, S. Hydrothermal Alteration and Past and Present Thermal Regimes in the Western Moat of Long Valley Caldera. *J. Volcanol. Geotherm. Res.* **1991**, *48*, 303–318. [CrossRef]
18. Inoue, A.; Kitagawa, R. Morphological Characteristics of Illitic Clay Minerals from a Hydrothermal System. *Am. Mineral.* **1994**, *79*, 700–711.
19. Patrier, P.; Papapanagiotou, P.; Beaufort, D.; Traineau, H.; Bril, H.; Rojas, J. Role of Permeability versus Temperature in the Distribution of the Fine (<0.2 Mm) Clay Fraction in the Chipilapa Geothermal System (El Salvador, Central America). *J. Volcanol. Geotherm. Res.* **1996**, *72*, 101–120. [CrossRef]
20. Vásquez, M.; Bauluz, B.; Nieto, F.; Morata, D. Illitization Sequence Controlled by Temperature in Volcanic Geothermal Systems: The Tinguiririca Geothermal Field, Andean Cordillera, Central Chile. *Appl. Clay Sci.* **2016**, *134*, 221–234. [CrossRef]
21. Beaufort, D.; Papapanagiotou, P.; Patrier, P.; Fouillac, A.M.; Traineau, H. I/S and C/S Mixed Layers, Some Indicators of Recent Physical-Chemical Changes in Active Geothermal Systems: The Case Study of Chipilapa (El Salvador). In Proceedings of the Seventeenth Workshop on Geothermal Reservoir Engineering, Stanford University, Stanford, CA, USA, 22–24 January 1996.
22. Maza, S.N.; Collo, G.; Morata, D.; Taussi, M.; Vidal, J.; Mattioli, M.; Renzulli, A. Active and Fossil Hydrothermal Zones of the Apacheta Volcano: Insights for the Cerro Pabellón Hidden Geothermal System (Northern Chile). *Geothermics* **2021**, *96*, 102206. [CrossRef]
23. Maza, S.N.; Collo, G.; Morata, D.; Cuña-Rodríguez, C.; Taussi, M.; Renzulli, A. The Hydrothermal Alteration of the Cordón de Inacaliri Volcanic Complex in the Framework of the Hidden Geothermal Systems within the Pabelloncito Graben (Northern Chile). *Minerals* **2021**, *11*, 1279. [CrossRef]

24. Rivera, G.; Morata, D.; Ramirez, C.; Volpi, G. Volcanic and Tectonic Evolution of Azufre–Inacaliri Volcanic Chain and Cerro Pabellón Geothermal Field (Northern Chile). In Proceedings of the World Geothermal Congress 2020+1, Reykjavik, Iceland, 24–27 October 2021.
25. Taussi, M.; Nisi, B.; Vaselli, O.; Maza, S.; Morata, D.; Renzulli, A. Soil CO₂ Flux and Temperature from a New Geothermal Area in the Cordón de Inacaliri Volcanic Complex (Northern Chile). *Geothermics* **2021**, *89*, 101961. [[CrossRef](#)]
26. Tibaldi, A.; Corazzato, C.; Rovida, A. Miocene–Quaternary Structural Evolution of the Uyuni–Atacama Region, Andes of Chile and Bolivia. *Tectonophysics* **2009**, *471*, 114–135. [[CrossRef](#)]
27. Tibaldi, A.; Bonali, F.L. Contemporary Recent Extension and Compression in the Central Andes. *J. Struct. Geol.* **2018**, *107*, 73–92. [[CrossRef](#)]
28. Veloso, E.E.; Tardani, D.; Elizalde, D.; Godoy, B.E.; Sánchez-Alfaro, P.A.; Aron, F.; Reich, M.; Morata, D. A Review of the Geodynamic Constraints on the Development and Evolution of Geothermal Systems in the Central Andean Volcanic Zone (18–28 Lat.S). *Int. Geol. Rev.* **2019**, *62*, 1294–1318. [[CrossRef](#)]
29. Giordano, G.; Pinton, A.; Cianfarra, P.; Baez, W.; Chiodi, A.; Viramonte, J.; Norini, G.; GropPELLI, G. Structural Control on Geothermal Circulation in the Cerro Tuzgle–Tocomar Geothermal Volcanic Area (Puna Plateau, Argentina). *J. Volcanol. Geotherm. Res.* **2013**, *249*, 77–94. [[CrossRef](#)]
30. Godoy, B.; Wörner, G.; Kojima, S.; Aguilera, F.; Simon, K.; Hartmann, G. Low-Pressure Evolution of Arc Magmas in Thickened Crust: The San Pedro–Linzor Volcanic Chain, Central Andes, Northern Chile. *J. S. Am. Earth Sci.* **2014**, *52*, 24–42. [[CrossRef](#)]
31. Morata, D.; Maza, S.N.; Vidal, J.; Taussi, M.; Renzulli, A.; Mattioli, M.; Pizarro, M.; Camus, E.; Godoy, B.; Alvear, B.; et al. Hydrothermal Alteration in Cerro Pabellón Geothermal Field: From Surface and Drill Core Data to Conceptual Model. In Proceedings of the World Geothermal Congress 2020+1, Reykjavik, Iceland, 24–27 October 2021.
32. Tassi, F.; Aguilera, F.; Darrah, T.; Vaselli, O.; Capaccioni, B.; Poreda, R.J.; Delgado Huertas, A. Fluid Geochemistry of Hydrothermal Systems in the Arica–Parinacota, Tarapacá and Antofagasta Regions (Northern Chile). *J. Volcanol. Geotherm. Res.* **2010**, *192*, 1–15. [[CrossRef](#)]
33. Giudetti, G.; Tempesti, L. First Geochemical Data from Cerro Pabellón Geothermal Project (Apacheta Region, Chile). In Proceedings of the World Geothermal Congress 2020+1, Reykjavik, Iceland, 24–27 October 2021.
34. Baccarin, F.; Volpi, G.; Rivera, G.; Giorgi, N.; Arias, A.; Giudetti, G.; Cei, M.; Cecioni, M.; Rojas, L.; Ramirez, C. Cerro Pabellón Geothermal Field (Chile): Geoscientific Feature and 3D Geothermal Model. In Proceedings of the World Geothermal Congress 2020+1, Reykjavik, Iceland, 24–27 October 2021.
35. Morata, D.; Reich, M.; Muñoz-Saez, C.; Daniele, L.; Rivera, G.; Volpi, G.; Cecioni, M.; Giudetti, G.; Cappetti, G. Origin and Age of Fluids at the Cerro Pabellón Geothermal System, Northern Chile. In Proceedings of the 41st New Zealand Geothermal Workshop, Auckland, New Zealand, 25–27 November 2019.
36. Bradford, J.; McLennan, J.; Moore, J.; Glasby, D.; Waters, D.; Kruwells, R.; Bailey, A.; Rickard, W.; Bloomfield, K.; King, D. Recent Developments at the Raft River Geothermal Field. In Proceedings of the Thirty-Eighth Workshop on Geothermal Reservoir Engineering, Stanford University, Stanford, CA, USA, 11 February 2013.
37. Davatzes, N.C.; Hickman, S.H. Controls on Fault-Hosted Fluid Flow; Preliminary Results from the Coso Geothermal Field, CA. In Proceedings of the Geothermal Resources Council Transactions, Geothermal Resources Council, Davis, CA, USA, 25 September 2005; Volume 29, pp. 343–348.
38. Genter, A.; Evans, K.; Cuenot, N.; Fritsch, D.; Sanjuan, B. Contribution of the Exploration of Deep Crystalline Fractured Reservoir of Soultz to the Knowledge of Enhanced Geothermal Systems (EGS). *C. R. Geosci.* **2010**, *342*, 502–516. [[CrossRef](#)]
39. Vidal, J.; Hehn, R.; Glaas, C.; Genter, A. How Can Temperature Logs Help Identify Permeable Fractures and Define a Conceptual Model of Fluid Circulation? An Example from Deep Geothermal Wells in the Upper Rhine Graben. *Geofluids* **2019**, *2019*, 3978364. [[CrossRef](#)]
40. Vidal, J.; Genter, A.; Chopin, F. Permeable Fracture Zones in the Hard Rocks of the Geothermal Reservoir at Rittershoffen, France. *J. Geophys. Res. Solid Earth* **2017**, *122*, 4864–4887. [[CrossRef](#)]
41. Brindley, G.W.; Brown, G. X-Ray Diffraction Procedures for Clay Mineral Identification. In *Crystal Structures of Clay Minerals and Their X-ray Identification*; Brindley, G.W., Brown, G., Eds.; Mineralogical Society: London, UK, 1980; Volume 5, pp. 305–360. ISBN 978-0-903056-37-3.
42. Wilson, M.J. *Rock-Forming Minerals, Sheet Silicates–Clay Minerals*, 2nd ed.; The Geological Society: London, UK, 2013; Volume 3C.
43. Foster, M.D. Studies of Celadonite and Glauconite. USGS Numbered Series. *Prof. Pap.* **1969**, *614F*, F1–F17. [[CrossRef](#)]
44. Beaufort, D.; Baronnet, A.; Lanson, B.; Meunier, A. Corrensite; A Single Phase or a Mixed-Layer Phyllosilicate in Saponite-to-Chlorite Conversion Series? A Case Study of Sancerre-Couy Deep Drill Hole (France). *Am. Mineral.* **1997**, *82*, 109–124. [[CrossRef](#)]
45. Moore, D.M.; Reynolds, R.C. *Identification of Clay Minerals and Associated Minerals*, 2nd ed.; Oxford University Press: Oxford, UK, 1997.
46. Koyama, K. Takeuchi Clinoptilolite: The Distribution of Potassium Atoms and Its Role in Thermal Stability. *Z. Für Krist.-Cryst. Mater.* **1977**, *145*, 216–239. [[CrossRef](#)]
47. Mansouri, N.; Rikhtegar, N.; Panahi, H.A.; Atabi, F.; Shahraki, B.K. Porosity, Characterization and Structural Properties of Natural Zeolite-Clinoptilolite-as a Sorbent. *Environ. Prot. Eng.* **2013**, *39*, 139–152.

48. Lowell, J.D.; Guilbert, J.M. Lateral and Vertical Alteration-Mineralization Zoning in Porphyry Ore Deposits. *Econ. Geol.* **1970**, *65*, 373–408. [[CrossRef](#)]
49. Thomasson, J.; Kristmannsdottir, H. High Temperature Alteration Minerals and Thermal Brines, Reykjanes, Iceland. *Contrib. Mineral. Petrol.* **1972**, *36*, 123–134. [[CrossRef](#)]
50. Beaufort, D.; Patrier, P.; Meunier, A.; Ottaviani, M.M. Chemical Variations in Assemblages Including Epidote and/or Chlorite in the Fossil Hydrothermal System of Saint Martin (Lesser Antilles). *J. Volcanol. Geotherm. Res.* **1992**, *51*, 95–114. [[CrossRef](#)]
51. López-Munguira, A.; Nieto, F.; Morata, D. Chlorite Composition and Geothermometry: A Comparative HRTEM/AEM-EMPA-XRD Study of Cambrian Basic Lavas from the Ossa Morena Zone, SW Spain. *Clay Miner.* **2002**, *37*, 267–281. [[CrossRef](#)]
52. Mas, A.; Guisseau, D.; Patrier Mas, P.; Beaufort, D.; Genter, A.; Sanjuan, B.; Girard, J.P. Clay Minerals Related to the Hydrothermal Activity of the Bouillante Geothermal Field (Guadeloupe). *J. Volcanol. Geotherm. Res.* **2006**, *158*, 380–400. [[CrossRef](#)]
53. Beaufort, D.; Rigault, C.; Billon, S.; Billault, V.; Inoue, A.; Inoue, S.; Patrier, P. Chlorite and Chloritization Processes through Mixed-Layer Mineral Series in Low-Temperature Geological Systems—A Review. *Clay Miner.* **2015**, *50*, 497–523. [[CrossRef](#)]
54. Gorini, A.; Ridolfi, F.; Piscaglia, F.; Taussi, M.; Renzulli, A. Application and Reliability of Calcic Amphibole Thermobarometry as Inferred from Calc-Alkaline Products of Active Geothermal Areas in the Andes. *J. Volcanol. Geotherm. Res.* **2018**, *358*, 58–76. [[CrossRef](#)]
55. Vidal, J.; Patrier, P.; Genter, A.; Beaufort, D.; Dezayes, C.; Glaas, C.; Lerouge, C.; Sanjuan, B. Clay Minerals Related to the Circulation of Geothermal Fluids in Boreholes at Rittershoffen (Alsace, France). *J. Volcanol. Geotherm. Res.* **2018**, *349*, 192–204. [[CrossRef](#)]
56. Glaas, C.; Patrier, P.; Vidal, J.; Beaufort, D.; Genter, A. Clay Mineralogy: A Signature of Granitic Geothermal Reservoirs of the Central Upper Rhine Graben. *Minerals* **2021**, *11*, 479. [[CrossRef](#)]
57. Nieto, F.; Abad, I.; Bauluz, B.; Reolid, M. Textural and Genetic Relationships between Glauconite and Celadonite at the Nanoscale: Two Different Structural-Compositional Fields. *J. Eur. J. Mineral.* **2021**, *33*, 503–517. [[CrossRef](#)]